ACS ES&T Engineering

pubs.acs.org/estengg

Article

Joule Heating-Induced Active Mg^0 into Nano-Mg Composites for Boosted Oxidation and Antiviral Performance

Xuan Wu,[‖] Yubing Jiao,[‖] Chao Jia, Liming Sun, Fengbo Yu, Litao Lin, Jie Gao, Tao Teng, Zhelin He, Aodi Li, Shicheng Zhang, Jinguang Yang, Shaobin Wang, and Xiangdong Zhu*

Cite This: *ACS EST Engg.* 2024, 4, 1302−1311

Read Online

ACCESS | Metrics & More | Article Recommendations | Supporting Information

ABSTRACT: Nano-Mg^0 composite has unlocked new avenues for organic contaminant removal and virus inactivation due to active magnesium in earth-abundance and eco-friendliness. However, the pyrolysis synthesis hinders the chemical activity of the as-prepared nano-Mg composite. Herein, we report instantaneous flash Joule heating (FJH) to introduce active Mg^0 to form a nano-Mg^0/MgO composite for active oxidation and antiviral performance. Mg^0 could be formed by FJH in milliseconds through Mg−O bond fracturing and thin aromatic-carbon layer deposition due to the rapid heating/cooling rate for blocking Mg^0 oxidation. It was found that the Mg^0 content was enhanced with an increasing pulsing voltage in preparation of the nano-Mg composite, finally improving both its oxidation and antiviral capabilities. Density functional theory calculations indicate that Mg^0 increases the binding affinity for an oxidant, thereby enhancing the oxidation capacity. A plaque reduction assay indicated that the nano-Mg^0/MgO composite directly inactivated herpes simplex virus type 2. Moreover, toward a large-scale production, we developed a continuous FJH automation apparatus to manufacture the nano-Mg^0/MgO composite, which offers a highly efficient platform for scale-up fabrication and wide applications.

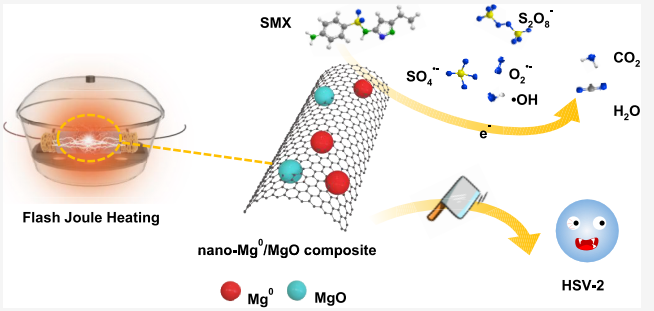

KEYWORDS: *nano-Mg^0/MgO composite, advanced oxidation processes, HSV-2 inactivation, flash Joule heating*

1. INTRODUCTION

Over the past decades, organic pollutant contamination and virus transmission in water have seriously threatened human health and environmental safety.[1,2] Particularly, the outbreak of pathogenic viruses has caused a global havoc, which brings the need for disinfection by effective methods.[3] Nanometal composites have burgeoned and strived to be promising materials to solve these problems.[4−7] Especially, Fe-based composites have been widely applied to the oxidation processes of organic pollutants due to their earth-abundant and inexpensive characteristics.[8−12] However, iron leaching beyond the self-degradation capacity of an ecosystem presents an environmental security risk (Figure 1a).[13−16] Although a series of methods, such as encapsulated Fe in a graphene shell or the introduction of a metal sacrificial agent, have been used to inhibit iron leaching, the rigorous synthetic conditions limit its wide application.[17,18] Additionally, other metals like silver (Ag), copper (Cu), and zinc (Zn) are widely recognized as antiviral metals,[19] yet they suffer from low abundance and high price. Recently, earth-abundant and eco-friendly magnesium (Mg) has led to the broad utilization prospects of nano-Mg composites in pollutant removal and antiviral applications.[20,21]

Conventional thermal treatments such as pyrolysis are important approaches to obtain nano-Mg composites, while Mg nanoparticles are prone to aggregate during the long heating process and result in low atom-utilization efficiency.[22,23] Moreover, the operation temperature (673−1273 K) used is prone to synthesize sole high valence Mg (such as MgO) as the temperature is not sufficient to break the Mg−O bond, thus limiting the formation of active Mg^0 components.[24,25] However, Mg^0 generally shows strong chemical reducibility and high activity.[20,26]

Herein, to solve these problems, we used a robust carbon-assisted flash Joule heating (FJH) reaction at a ultrahigh temperature (~2800 K in milliseconds) to produce Mg^0 in a nano-Mg composite.[27] First, the decomposition reaction from a Mg salt (such as $Mg(CH_3COO)_2$) to MgO occurred during a low-temperature stage of the FJH reaction (~600 K).[28] Subsequently, the Mg−O bond was broken due to the decomposition and carbothermic reduction reactions at above 2000 K, which induced the formation of Mg^0

Received: December 20, 2023
Revised: April 15, 2024
Accepted: April 15, 2024
Published: April 24, 2024

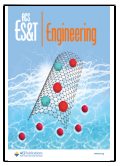

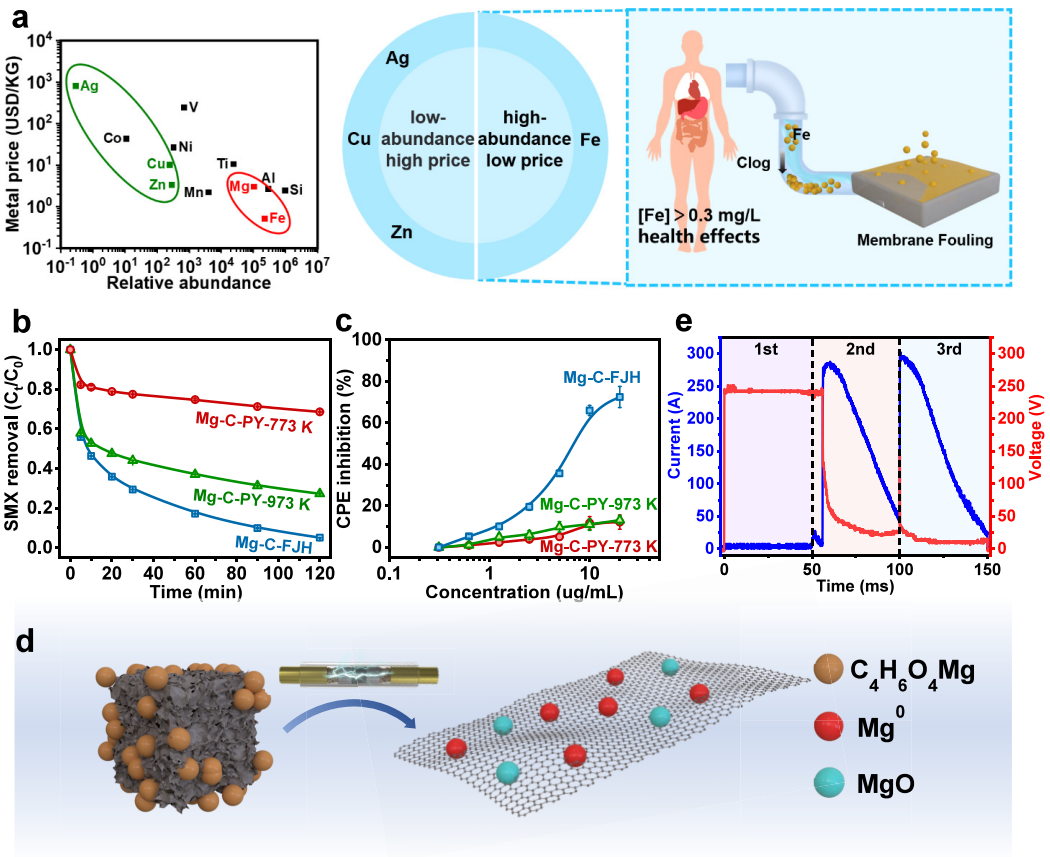

Figure 1. Synthesis of nano-Mg^0/MgO composites and degradation performance of SMX by different nano-MgO composites. (a) Relationship between metal price and its relative abundance in the Earth, advantages, and disadvantages of Ag, Cu, Zn, Mg, Fe, and AI. (The relative abundance data come from https://ptable.com, based on abundance of Si: 10^6 atoms. The metal price data on August 2, 2023 come from https://www.metal.com.). (b) SMX degradation profiles of nano-Mg composite derived from flash Joule heating (Mg−C−FJH) and pyrolysis (Mg−C−PY) technologies (experiment conditions: $[Mg-C-FJH]_0 = [Mg-C-PY]_0 = 1$ g/L, $[SMX]_0 = 10$ mg/L, $[PDS]_0 = 5$ mM). (c) Antiviral activity of Mg−C−PY and Mg−C−FJH against HSV-2. (d) Schematic diagram for the preparation process of Mg−C−FJH. (e) Recorded current and voltage in the FJH process via an oscilloscope (RIGOL, DS1104Z Plus).

nanoparticles.[29] Additionally, the rapid heating and cooling can result in the formation of a thin aromatic-carbon layer deposition, thus blocking the oxidation of Mg^0.[30,31] Moreover, to realize a scale-up synthesis of nanocomposite by FJH technology, we designed a continuous FJH automation apparatus to continuously produce a nano-Mg^0/MgO composite at a large scale.

Sulfamethoxazole (SMX) and herpes simplex virus type 2 (HSV-2) widely exist as antimicrobial agents and enveloped virus, respectively. Moreover, they are found to be widely present in wastewater.[32,33] Therefore, the nano-Mg^0/MgO composite in activating peroxydisulfate (PDS) to degrade SMX was studied to understand the structure−property relationships. In addition, HSV-2 inactivation by the nano-Mg^0/MgO composite was studied further to confirm its antiviral process. Finally, the FJH automation apparatus further sheds light on the scale-up of nanocomposite fabrication and provides a significant basis for large-scale applications.

2. MATERIALS AND METHODS

2.1. Batch and Continuous Flash Joule Heating for Synthesis of Nano-Mg^0/MgO Composites. Magnesium acetate tetrahydrate ($Mg(CH_3COO)_2{\cdot}4H_2O$) and a carbon substrate (hydrochar) with the same weight were first mixed. Hydrochar was used to provide sufficient Joule heat, thus assisting the FJH process.[34] Then, 10 wt % carbon black (conductive additive) was added to minimize the sample resistance to ∼100 Ω for successfully starting the FJH reaction. The Mg loading of such a raw material was ∼5.1 wt % unless else stated. Lastly, this mixed material was packed in a quartz tube with an inner diameter of 6 mm and compressed with copper and graphite electrodes for a batch FJH reaction under a mild vacuum. Notably, the structural properties of these obtained materials can be tailored by adjusting the FJH pulsing voltage (150−250 V) and discharge time (50−150 ms).

To enhance the productivity of the nano-Mg^0/MgO composite, we further designed a continuous FJH automation apparatus. Different from the batch FJH apparatus, the designed automation apparatus was controlled by a programmable logic controller-controlled integrated system, including an electrical control panel, a loading and collecting tray, robot arms, and a reaction chamber. Quartz tubes (10 mm of inner diameter) containing a mixed material were first arranged in the loading tray, and one robot arm then transported such a mixed material to the reaction chamber in turn. A movable sleeve was achieved to provide a negative pressure environment for the FJH reaction. Then, the sample is assigned to the appropriate voltage (250 V) with ∼100 ms due to the increased resistance. Notably, one-time extended shock was more helpful for automated production. Finally, the robot arm

https://doi.org/10.1021/acsestengg.3c00614
ACS EST Engg. 2024, 4, 1302−1311

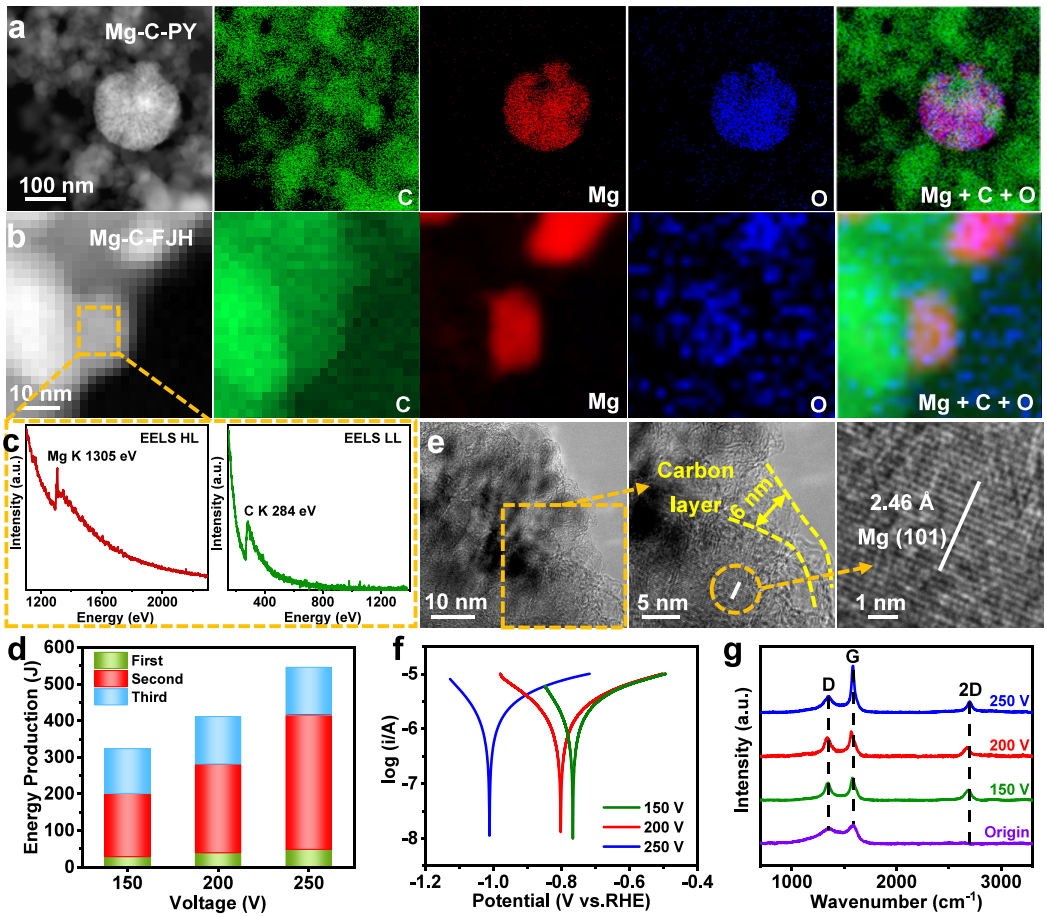

Figure 2. Morphology and surface chemical property analysis of nano-Mg composites. (a) HAADF images and EDX elemental mapping of Mg−C−PY-973 K. (b) HAADF images and EELS elemental distribution of Mg−C−FJH prepared at a pulsing voltage of 250 V. (c) EELS spectrum of magnesium K edge and carbon K edge. (d) Energy production recorded during the Mg−C−FJH synthesis process at different pulsing voltages. (e) HR-TEM images of Mg−C−FJH at a pulsing voltage of 250 V. (f) Tafel curves of Mg−C−FJH prepared at different pulsing voltages. (g) Raman spectra of the precursor of Mg−C−FJH and Mg−C−FJH prepared at different pulsing voltages.

further transferred the prepared composite to the collecting tray.

2.2. Oxidation and HSV-2 Inactivation by Nano-Mg^0/MgO Composites. The oxidation capacity of a nano-Mg^0/MgO composite was evaluated by activating PDS to degrade SMX. The SMX oxidation reactions were initiated by the simultaneous addition of 1 g/L nano-Mg^0/MgO composite and 5 mM PDS containing SMX under shaking at 298 K. Then, the reaction suspension was withdrawn at a desired interval and filtered immediately through a 0.22 μm membrane for quantitative analysis. The concentrations of SMX were detected by high-performance liquid chromatography (HPLC, Agilent 1260 Infinity II) with a symmetry C18 column at a wavelength of 265 nm. A mixture of 0.1% formic acid and methanol (volume/volume = 65/35) was adopted as the mobile phase with a flow rate of 1 mL/min.

The virus inactivation was directly evaluated by a plaque reduction assay of HSV-2. HSV-2 (50−100 PFU/well) was preincubated with or without a nano-Mg^0/MgO composite before infection. Then, the HSV-2 and nano-Mg^0/MgO composite mixture was transferred to Vero cell monolayers in six-well plates and incubated with gentle shaking. After removing the inoculum, cells were incubated at 310 K in agar overlay media. The cells were last fixed with 4% paraformaldehyde and stained with 1% crystal violet for plaque scanning and counting. More details can be found in the Supporting Information.

2.3. Characterizations of Flash Joule Heating-Induced Nano-Mg^0/MgO Composites. The crystalline structures of the nano-Mg^0/MgO composite were determined by X-ray diffraction (XRD, Ultima IV, Rigaku, Japan). The valence state of the Mg element for the as-prepared samples was obtained using X-ray photoelectron spectroscopy (XPS, Thermo Scientific K-Alpha, USA). Raman spectra were recorded with an XploRA Raman spectrometer with a 532 nm (5 mW) laser source under a 50× objective microscope. The morphologies were examined by transmission electron microscopy (TEM, FEI Tecnai F20). Dispersive X-ray spectroscopy (EDX) was conducted to prove the existence of C, Mg, and O, and individual atoms can be discerned in the high-angle annular dark-field (HAADF) images. Moreover, chemical analysis of Mg^0 was detected by transmission electron microscopy with double aberration correctors (Microscope Themis Z), and electron energy loss spectroscopy (EELS) was conducted to map the abundance of C and Mg elements in the as-prepared composite. It should be noted that the nano-Mg^0/MgO composite was directly coated on a copper screen to avoid the oxidation of Mg^0 during the EELS analysis. More details can be found in the Supporting Information.

https://doi.org/10.1021/acsestengg.3c00614
ACS EST Engg. 2024, 4, 1302−1311

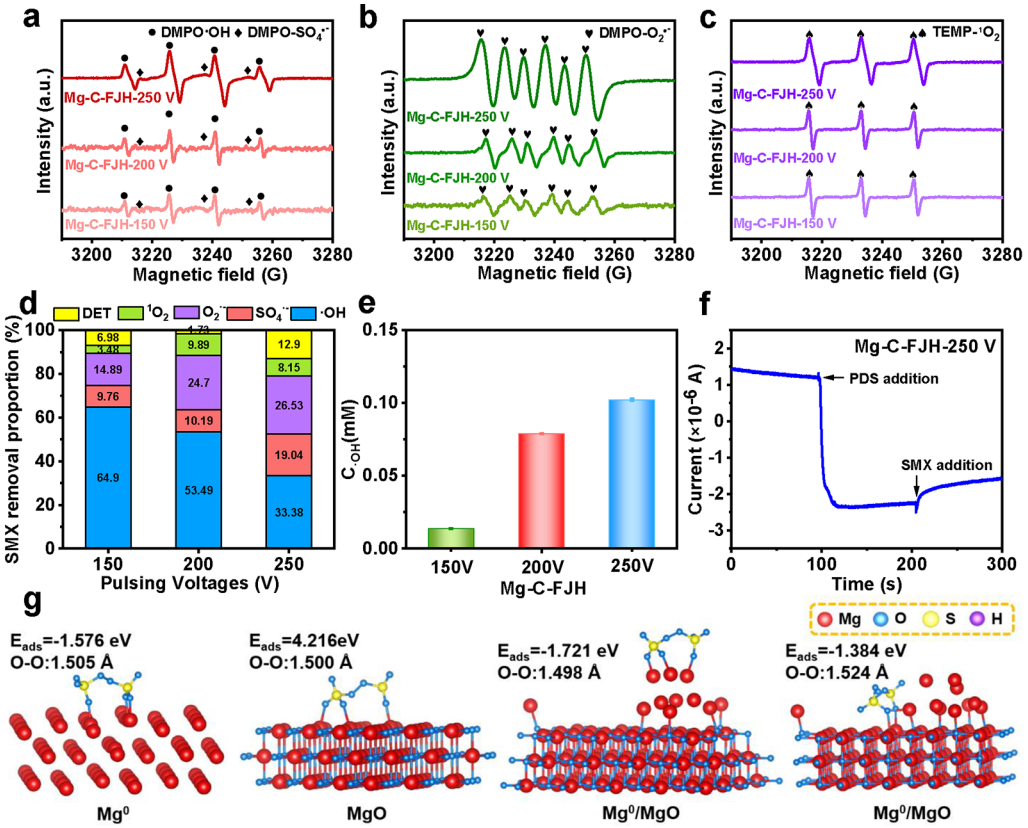

Figure 3. Advanced oxidation mechanism of Mg−C−FJH. EPR spectra of (a) •OH, $SO_4^{\bullet-}$, (b) $O_2^{\bullet-}$, and (c) $^1O_2$ in Mg−C−FJH at a pulsing voltage of 250 V and PDS system. (d) SMX degradation proportions of •OH, $O_2^{\bullet-}$, $SO_4^{\bullet-}$, and nonradical pathway in the Mg−C−FJH and PDS system. (e) Amount of •OH produced by the Mg−C−FJH and PDS system. (f) *I*−*t* curve of Mg−C−FJH prepared at a pulsing voltage of 250 V by adding PDS and SMX successively. (g) Optimized adsorption structure systems of different components with PDS.

3. RESULTS AND DISCUSSION

3.1. Flash Joule Heating for Production of an Active Nano-Mg Composite. Having earth-abundant and eco-friendly characteristics, the Mg-containing composite attracted considerable attention but showed disappointing oxidation performance.[26,35] This is because the chemical activity prepared by conventional pyrolysis was restricted by sole high valence Mg (MgO) and no zero valence Mg (Mg^0).[20,26,36] Specifically, the nano-Mg composite (Mg−C−PY) derived from the slow pyrolysis at two typical temperatures (773 and 973 K) showed a limited capacity (31.4 and 72.6%) on SMX removal by using PDS as the oxidant (Figure 1b). That is because the metal component in the nano-Mg composite from pyrolysis was mainly composed of MgO,[20,26] as confirmed by the XRD (Figure S1). Notably, agglomerated MgO leads to poor oxidation performance. In addition, the nano-Mg composite derived from pyrolysis at 773 and 973 K showed a weak antiviral effect against HSV-2, with only 12.1 and 13.1% inhibition, respectively (Figure 1c). Notably, the composite exhibited no significant cytotoxicity toward Vero cells (Figure S2).

To overcome these conventional technical defects, we introduced the FJH reaction to improve the structure, chemical reactivity, and antiviral capability of the nano-Mg composite. Excitingly, the oxidation capacity of SMX in the FJH derived nano-Mg composite (Mg−C−FJH) assisted by PDS can reach 98.8% (Figure 1b). The inhibition on HSV-2 reached 72.4% at a low concentration of Mg−C−FJH, with a higher potency comparable to that of the reference drug acyclovir (~40.7%) (Figure 1c). The synthesis strategy for Mg−C−FJH is briefly illustrated in Figure 1d and Figure S3. A transient voltage was applied, producing dazzling light that instantaneously raised the temperature to approximately 2800 K (Figure 1e and Figures S4−6), which is likely to induce new components in Mg−C−FJH for enhanced oxidation and viral inactivation performance.

3.2. Mg^0 Induced by Flash Joule Heating in Nano-Mg Composites. To understand the improved reactivity of Mg−C−FJH, we performed various structural analyses. The Mg component of Mg−C−FJH was uniformly distributed along the carbon substrates based on HAADF images and EDX elemental mapping (Figure S7). The Mg average size of Mg−C−FJH was approximately 10.8 nm (Figure S8). Meanwhile, Mg−C−PY was composed of approximately agminated MgO nanoparticles (200 nm) loaded on the carbon layer (Figure 2a). This difference indicated that the wide dispersion and small size of the Mg nanoparticles derived from FJH could provide more active sites to bolster chemical reactivity.[37]

Furthermore, clear lattice stripes in the high-resolution transmission electron microscopy (HR-TEM) images showed that Mg−C−FJH was composed of Mg^0 (101) and MgO (200) (Figure S9), and the same crystalline lattices were observed in the XRD patterns (Figure S10). Evidently, $Mg(CH_3COO)_2$ can easily decompose to MgO at low temperatures (573−673 K) (Figure 2a),[28] and Mg^0 was formed in milliseconds from the fast-breaking Mg−O bond due to decomposition or carbothermic reduction reactions at the temperature up to approximately 2000 K.[25] Consequently,

https://doi.org/10.1021/acsestengg.3c00614
ACS EST Engg. 2024, 4, 1302−1311

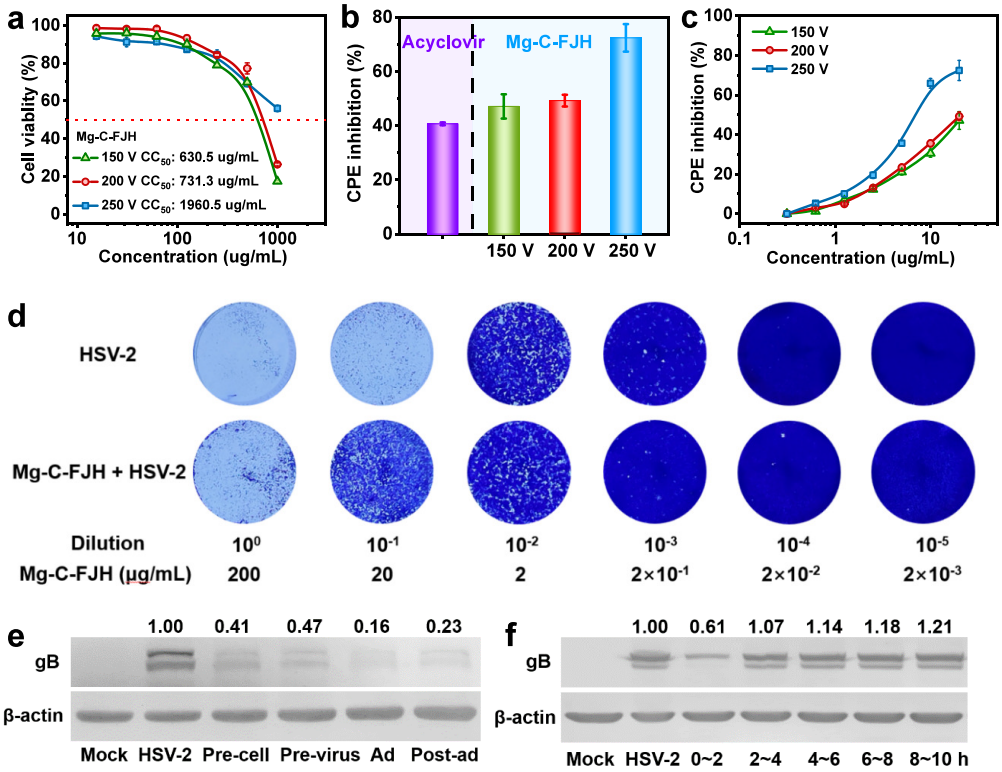

Figure 4. Antiviral activity of Mg−C−FJH against HSV-2. (a) The cytotoxicity of Mg−C−FJH in Vero cells was determined by MTT assay after 48 h of incubation (Mg−C−FJH were prepared at 150, 200, and 250 V pulsing voltages). (b) Antiviral activity of Mg−C−FJH against HSV-2 with acyclovir as the negative contrast and determined by the CPE inhibition assay. (c) Antiviral activity of Mg−C−FJH against HSV-2 in the CPE inhibition assay. (d) Inhibitory effects of Mg−C−FJH prepared at a pulsing voltage of 250 V on HSV-2 in vitro. HSV-2 (50−100 PFU/well) was preincubated with Mg−C−FJH and then transferred to Vero cells and subjected to a plaque reduction assay. (e) Expressions of glycoprotein B (gB) protein under four different treatment methods (pretreatment of virus, pretreatment of cells, adsorption, and postadsorption) were detected by Western blotting. (f) Expressions of gB protein under different time intervals (Mg−C−FJH was added at different time intervals of HSV-2 and cell contact) were detected by Western blotting. Blots were also probed for the β-actin protein as loading controls. The band intensity was quantified with ImageJ.

Mg^0 nanoparticles derived from FJH were directly observed from the HAADF images and EELS elemental distribution (Figure 2b). Figure 2c presents EELS spectra of magnesium K edge at 1305 eV and carbon K edge at 284 eV; the absence of an O peak at 534 eV indicated no O in this range, supporting the existence of Mg^0. Synchronously, the rapid heating and cooling rate ($\sim 10^2$ K/ms) realized the deposition of a thin aromatic-carbon layer to sustain the Mg^0 nanoparticles (Figure 2e and Figure S11).[6]

Additionally, the ratios of Mg^0 to Mg^{2+} in the Mg 1s XPS spectra of Mg−C−FJH increased from 14.7 to 52.7% as the pulsing voltage increased from 150 to 250 V (Figure S12). This is because the increased power and energy induced a higher reaction temperature (Figures S3−5 and S14−17), thus producing more Mg^0 species. Moreover, the corrosion potential in the Tafel results showed that the increasing Mg^0 component directly led to fast electron transport (Figure 2g). The Mg^0 was also reported to play the role of active component according to previous studies,[38,39] indicating that Mg^0 has potential to enhance the oxidation and antiviral performance of the as-prepared composite.

The role of carbon substrates was investigated, and the existence of a conjugated aromatic structure was found according to the observation of a $\pi-\pi$ transition. The C/O ratio increased in the C 1s XPS spectra with the increasing pulsing voltage (Figure S18).[40] In addition, a low-intensity D peak in the Raman spectra indicated the absence of defects. The decreased ratio of I_D/I_G values indicated a higher level of graphitization owing to the increased pulsing voltage (Figure 2f and Table S1).[40−42] These results suggest that the aromatic-carbon layer was favorable for electron transfer, thus enhancing the chemical reaction.[6]

3.3. Oxidation Mechanism of Flash Joule Heating-Induced Nano-Mg^0/MgO Composites. As shown in Figure 1b, Mg−C−FJH with a pulsing voltage of 250 V exhibited a superior SMX oxidation efficiency, implying that the Mg^0 component could markedly boost PDS activation. Notably, adsorption by Mg−C−FJH or PDS degradation alone was excluded because of the negligible SMX removal efficiency (Figure S19). Subsequently, the factors underlying the superior oxidation performance of Mg−C−FJH were further investigated. Strikingly, the oxidation performance of Mg−C−FJH increased with the increasing pulsing voltage during the preparation process, indicating that the increasing Mg^0 component played an important role in the oxidation process (Figure S20).

The degradation mechanism of SMX was further analyzed by electron paramagnetic resonance (EPR) and quenching experiments (Figure 3a−e and Figure S21−23). EPR results first indicated that the reactive oxygen species included •OH, SO_4•$^-$, O_2•$^-$, and $^1O_2$ (Figure 3a−c). Especially, •OH was the main contributor for SMX removal, and the contribution of

https://doi.org/10.1021/acsestengg.3c00614
ACS EST Engg. 2024, 4, 1302−1311

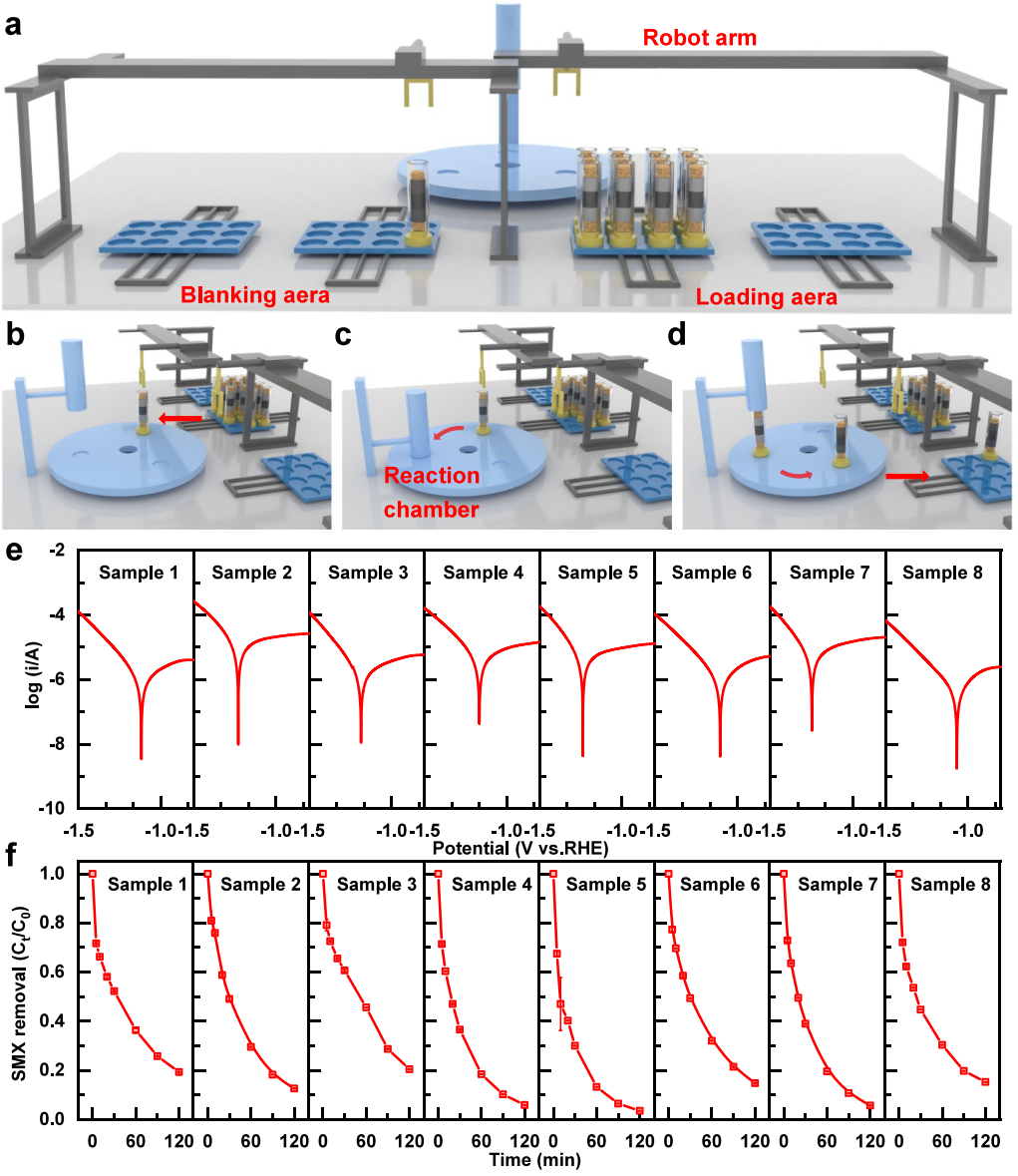

Figure 5. Continuous automated fabrication of Mg−C−FJH. (a) Schematic of the automation device for continuous production of the Mg−C−FJH. (b−d) Operation flowchart of automation apparatus. (e) Tafel curves of the Mg−C−FJH prepared from the automation apparatus. (f) Removal of SMX in PDS activated by Mg−C−FJH prepared from the automation apparatus.

•OH was decreased with increasing the pulsing voltage from 150 to 250 V (Figure 3d and Tables S3−5). The reason may be because the •OH concentration was slightly increased with the pulsing voltage at 250 V, while more SO_4•$^-$ and O_2•$^-$ were produced for SMX removal (Figures 3d,e). It should be noted that •OH, SO_4•$^-$, and O_2•$^-$ produced by C-FJH and the PDS system were excluded (Figure S24). Moreover, when the PDS and SMX were added into the electrolyte, the current was rapidly degressive and uplifted due to the electron transfer effects (Figure 3f). This result indicated that direct electron transfer (DET) of Mg−C−FJH with a pulsing voltage of 250 V was also assisted due to the enhanced Mg^0 contents and graphitization of the carbon substrate.[43] Thus, •OH was the main contributor for SMX oxidation performance, and more SO_4•$^-$, O_2•$^-$, and $^1O_2$ were produced, with the DET pathway enhanced by the prepared composites at a higher pulsing voltage (Figure S25). The degradation pathway of SMX was further investigated. The chromatographs of GC-MS and LC-MS for analyzing the degradation pathway of SMX are shown in Tables S6 and S7, respectively. As shown in Figure S26, the amino oxidation and methylation process were detected in the degradation pathway of SMX;[44−46] the C−N bond, S−N bond, and S−C bond were also easily broken to form intermediate products,[47−49] which further formed acid and then completely mineralized to produce H_2O, CO_2, CO_3^{2-}, H_2SO_4, H_2SO_3, and NO_3^-.[50]

Furthermore, the role of Mg^0 in SMX oxidation was rationalized by using density functional theory (DFT) calculations. Mg^0 and MgO were used as benchmark models, and some Mg atoms were placed in the MgO model to form a Mg^0/MgO bicomponent model (Figure 3g). By inducing active Mg^0, the adsorption energy of PDS on the Mg^0 site in Mg^0/MgO (−1.721 eV) was lower than single Mg^0 (−1.576 eV) and Mg^{2+} of MgO (4.216 eV). Evidently, the lower adsorption energy contributes to the enhanced oxidation performance of Mg^0/MgO. In addition, the O−O bond lengths

https://doi.org/10.1021/acsestengg.3c00614
ACS EST Engg. 2024, 4, 1302−1311

of PDS on Mg^{2+} of Mg^0/MgO (1.524 Å) was longer than on Mg^0 (1.505 Å) and Mg^{2+} of MgO (1.500 Å). That demonstrated that the Mg^0/MgO composite helped attract electron clouds from PDS, thus enhancing their adsorption affinity. Mg^0/MgO easily adsorbed PDS and broke the O−O bond to produce radicals owing to the increased electron transmission ability, which considerably improved the oxidation properties.

Owing to the protective role of the aromatic-carbon substrate, Mg−C−FJH exhibited extraordinary stability, as confirmed by high SMX removal reactivity even though the composite was exposed to air for 3 months (Figure S27). Additionally, the activity of Mg−C−FJH in activating PDS to oxidize SMX showed the advantages of FJH technology as compared to that of several reported catalysts (Figure S28 and Table S2).[33,51−53] Mg−C−FJH also exhibited significant SMX removal efficiency over a wide pH range and in different oxidation systems, which provides a wider scope for its application (Figures S29 and 30).

3.4. HSV-2 Inactivation by Flash Joule Heating-Induced Nano-Mg^0/MgO Composites. Considering the antiviral performance of Mg,[54,55] we focused on the HSV-2 inactivation performance of Mg−C−FJH. We first eliminated the cytotoxicity of the nano-Mg^0/MgO composite according to the observation that the composite exhibited no significant cytotoxicity in Vero cells at a low dose (0−100 μg/mL) (Figure 4a). The HSV-2 inhibition effect of Mg−C−FJH was superior to that of acyclovir, which was recognized as a negative contrast, indicating the excellent antiviral performance of the composite.[56] Moreover, the antiviral capability increased with the enhanced pulsing voltage for the preparation, which means that the antiviral capability is likely to be improved by increasing the Mg^0 content (Figure 4b,c).

Strikingly, the antiviral efficacy of Mg−C−FJH against HSV-2 infectivity was first evaluated by a plaque reduction assay *in vitro*. The number of HSV-2 plaques was markedly reduced through the preincubation of HSV-2 with Mg−C−FJH compared with the HSV-2 control group, as visually observed in Figure 4d to confirm that Mg−C−FJH could directly inactivate HSV-2 particles. In addition, a time-dependent assay showed the stage for the composite to exert its inhibitory actions *in vitro*.[57] The Western blotting and cytopathic effect (CPE) inhibition assay clearly confirmed that the inhibition of HSV-2 infection by the nano-Mg^0/MgO composite occurred mainly at the adsorption stage of Vero cells infected with HSV-2 (Figure 4e and Figures S31 and S32). Furthermore, Mg−C−FJH also exhibited excellent HSV-2 inactivation performance during the initial contact phase between HSV-2 and the cells (0−2 h; Figure 4f and Figures S33 and S34). Thus, the Mg−C−FJH could directly inactivate the virus, specifically at the initial adsorption stage of HSV-2.

3.5. Continuous Joule Heating for Nano-Mg^0/MgO Composite Fabrication. Although the FJH reaction is ultrafast, the manual loading and blanking processes prolong the sample preparation time. To enhance the apparatus's production efficiency and progress from the laboratory to scalable production, we developed a continuous FJH automation apparatus to produce large quantities of nanocomposites (Figure 5a and Figure S35). A programmable logic controller-controlled integrated apparatus was designed via three modular components: electrical control, mechanical control, and the FJH reaction. The FJH reaction parameters, including reaction time and pulsing voltage, were set using an electrical control module. Instead of manual loading and blanking in the mechanical control module, two robot arms were used to achieve the continuous transfer of samples. Then, the opening and closure of the FJH reaction chamber using a movable sleeve require a negative pressure environment for the reaction. The automation system achieved continuous production of Mg−C−FJH (Figure 5b−d).

Interestingly, the productivity can reach approximately 40 times more than that of laboratory batch FJH devices owing to automatic mechanical control and FJH reaction modules (Table S6). Notably, production efficiency can be further enhanced by magnifying the capacitance of the apparatus and increasing the sample load. The cost of Mg−C−FJH production was estimated to be 1452.5 USD/ton (including material and energy costs), which is twofold less than that of commercial Mg^0 (3010.0 USD/ton), promoting broad use in practical applications (Table S4).

Furthermore, we tentatively tested the stability and oxidation performance of eight samples. The preparation parameters, including the pulsing voltage, current, power, and energy production, showed a relatively stable reaction process (Figures S36−38). Accordingly, the stable and negative corrosion potential (−1.0 to −1.24 V) of these samples indicated that Mg^0 contributed to the fast electron transport ability of Mg−C−FJH (Figure 5e). This directly contributed to the high oxidation capacity on SMX by activating PDS (79.5−96.5%) (Figure 5f). It should be noted that the difference between the eight samples can be attributed to the nonuniform electric shock on the samples, which can be ignored by the mixture of a large number of as-prepared samples. Undoubtedly, Mg−C−FJH showed remarkable electron transport ability and oxidation properties, demonstrating the great potential of the continuous FJH automation apparatus for the large-scale synthesis of nanocomposites.

4. CONCLUSIONS

We report an instantaneous FJH technology for induced activity Mg^0 into nano-Mg composites to break through the disadvantages of conventional pyrolysis methods. Mg^0 was formed by FJH in milliseconds through Mg−O bond fracturing, and thin aromatic-carbon layer deposition was due to the rapid heating/cooling rate for blocking Mg^0 oxidation. The active Mg^0 enhanced the PDS activation to produce highly reactive oxygen species (like •OH), thus exhibiting a remarkable SMX oxidation efficiency. DFT calculations indicated that the induced activity Mg^0 could increase the binding affinity with oxidants, thus enhancing the oxidation capacity. Additionally, the increasing Mg^0 component also improved the HSV-2 inactivation capability of Mg−C−FJH. Moreover, a continuous FJH automation apparatus was designed to continuously produce nanocomposites, which makes the large-scale application of nanocomposites possible. In this way, this work opens up a new avenue to continuously prepare different active nanometal composites and also provides new insights into organic depollution and virus inactivation in water systems.

■ ASSOCIATED CONTENT

Supporting Information

The Supporting Information is available free of charge at https://pubs.acs.org/doi/10.1021/acsestengg.3c00614.

https://doi.org/10.1021/acsestengg.3c00614
ACS EST Engg. 2024, 4, 1302−1311

Parameters of the material synthesis process, including flash current, voltage, and fitting temperature; material characterization, including TEM images, XRD analysis, and XPS analysis; experiments on the degradation of SMX under different conditions, including different scavengers, different pH, and different oxidation systems; EPR spectra of reactive oxygen species; antiviral activity of the material, including CPE inhibition and gB protein level; and parameters of the continuous material synthesis process, including flash current and voltage (PDF)

AUTHOR INFORMATION

Corresponding Author

Xiangdong Zhu − *Department of Environmental Science and Engineering, Fudan University, Shanghai 200092, China;* orcid.org/0000-0002-8536-7690; Email: zxdjewett@fudan.edu.cn

Authors

Xuan Wu − *Department of Environmental Science and Engineering, Fudan University, Shanghai 200092, China*

Yubing Jiao − *Tobacco Research Institute of Chinese Academy of Agricultural Sciences, Qingdao 266000, China;* orcid.org/0009-0001-5663-1106

Chao Jia − *Department of Environmental Science and Engineering, Fudan University, Shanghai 200092, China*

Liming Sun − *Department of Environmental Science and Engineering, Fudan University, Shanghai 200092, China*

Fengbo Yu − *Department of Environmental Science and Engineering, Fudan University, Shanghai 200092, China*

Litao Lin − *Department of Environmental Science and Engineering, Fudan University, Shanghai 200092, China*

Jie Gao − *Department of Environmental Science and Engineering, Fudan University, Shanghai 200092, China*

Tao Teng − *Department of Environmental Science and Engineering, Fudan University, Shanghai 200092, China*

Zhelin He − *Department of Environmental Science and Engineering, Fudan University, Shanghai 200092, China*

Aodi Li − *Department of Environmental Science and Engineering, Fudan University, Shanghai 200092, China*

Shicheng Zhang − *Department of Environmental Science and Engineering, Fudan University, Shanghai 200092, China;* orcid.org/0000-0001-9994-1385

Jinguang Yang − *Tobacco Research Institute of Chinese Academy of Agricultural Sciences, Qingdao 266000, China;* orcid.org/0000-0002-9584-9634

Shaobin Wang − *School of Chemical Engineering, The University of Adelaide, Adelaide, SA 5005, Australia;* orcid.org/0000-0002-1751-9162

Complete contact information is available at: https://pubs.acs.org/10.1021/acsestengg.3c00614

Author Contributions

‖X.W. and Y.B.J. contributed equally to this paper.

Notes

The authors declare no competing financial interest.

ACKNOWLEDGMENTS

This work was supported by a fund from the National Natural Science Foundation of China (No. 22276040), the special fund of state environmental protection engineering center for urban soil contamination control and remediation (USCR-202204), and leading project of Bai Ma future food research institute (JBGS-2021-007). We acknowledge the use of facilities within the State Key Laboratory of Surface Physics and Department of Physics at Fudan University.

REFERENCES

(1) Hodges, B. C.; Cates, E. L.; Kim, J. H. Challenges and prospects of advanced oxidation water treatment processes using catalytic nanomaterials. *Nat. Nanotechnol.* **2018**, *13* (8), 642−650.

(2) Bibby, K.; Crank, K.; Greaves, J.; Li, X.; Wu, Z.; Hamza, I. A.; Stachler, E. Metagenomics and the development of viral water quality tools. *NPJ. Clean Water* **2019**, *2* (1), 9.

(3) Huang, R.; Ma, C.; Huangfu, X.; Ma, J. Preparing for the next pandemic: Predicting UV inactivation of coronaviruses with machine learning. *Environ. Sci. Technol.* **2023**, *57* (37), 13767−13777.

(4) Kumar, A.; Dutta, S.; Kim, S.; Kwon, T.; Patil, S. S.; Kumari, N.; Jeevanandham, S.; Lee, I. S. Solid-state reaction synthesis of nanoscale materials: Strategies and applications. *Chem. Rev.* **2022**, *122* (15), 12748−12863.

(5) Xin, Q.; Shah, H.; Nawaz, A.; Xie, W.; Akram, M. Z.; Batool, A.; Tian, L.; Jan, S. U.; Boddula, R.; Guo, B.; Liu, Q.; Gong, J. R. Antibacterial carbon-based nanomaterials. *Adv. Mater.* **2019**, *31* (45), e1804838.

(6) Xie, H.; Liu, Y.; Li, N.; Li, B.; Kline, D. J.; Yao, Y.; Zachariah, M. R.; Wang, G.; Su, D.; Wang, C.; Hu, L. High-temperature-pulse synthesis of ultrathin-graphene-coated metal nanoparticles. *Nano Energy* **2021**, *80*, No. 105536.

(7) Markova, Z.; Siskova, K. M.; Filip, J.; Cuda, J.; Kolar, M.; Safarova, K.; Medrik, I.; Zboril, R. Air stable magnetic bimetallic Fe-Ag nanoparticles for advanced antimicrobial treatment and phosphorus removal. *Environ. Sci. Technol.* **2013**, *47* (10), 5285−5293.

(8) Guan, X.; Sun, Y.; Qin, H.; Li, J.; Lo, I. M.; He, D.; Dong, H. The limitations of applying zero-valent iron technology in contaminants sequestration and the corresponding countermeasures: The development in zero-valent iron technology in the last two decades (1994−2014). *Water Res.* **2015**, *75*, 224−248.

(9) Hu, Y.; Peng, X.; Ai, Z.; Jia, F.; Zhang, L. Liquid nitrogen activation of zero-valent iron and its enhanced Cr(VI) removal performance. *Environ. Sci. Technol.* **2019**, *53* (14), 8333−8341.

(10) Ling, L.; Huang, X.; Li, M.; Zhang, W. X. Mapping the reactions in a single zero-valent iron nanoparticle. *Environ. Sci. Technol.* **2017**, *51* (24), 14293−14300.

(11) Ling, L.; Zhang, W. X. Enrichment and encapsulation of uranium with iron nanoparticle. *J. Am. Chem. Soc.* **2015**, *137* (8), 2788−2791.

(12) Shen, W.; Kang, H.; Ai, Z. Comparison of aerobic atrazine degradation with zero valent aluminum and zero valent iron. *J. Hazard. Mater.* **2018**, *357*, 408−414.

(13) Haldar, D.; Duarah, P.; Purkait, M. K. MOFs for the treatment of arsenic, fluoride and iron contaminated drinking aater: A review. *Chemosphere* **2020**, *251*, No. 126388.

(14) Khatri, N.; Tyagi, S.; Rawtani, D. Recent strategies for the removal of iron from water: A review. *J. Water Process. Eng.* **2017**, *19*, 291−304.

(15) Jafari, M.; Vanoppen, M.; van Agtmaal, J. M. C.; Cornelissen, E. R.; Vrouwenvelder, J. S.; Verliefde, A.; van Loosdrecht, M. C. M.; Picioreanu, C. Cost of fouling in full-scale reverse osmosis and nanofiltration installations in the netherlands. *Desalination* **2021**, *500*, No. 114865.

(16) Dong, H.; Gao, B.; Yue, Q.; Sun, S.; Wang, Y.; Li, Q. Floc properties and membrane fouling of different monomer and polymer Fe coagulants in coagulation-ultrafiltration process: The role of Fe (III) species. *Chem. Eng. J.* **2014**, *258*, 442−449.

(17) Cui, L.; Zhao, X.; Xie, H.; Zhang, Z. Overcoming the activity-stability trade-off in heterogeneous electro-fenton catalysis: Encapsu-

lating carbon cloth-supported iron oxychloride within graphitic layers. *ACS Catal.* **2022**, *12* (21), 13334−13348.
(18) Bao, Y.; Lian, C.; Huang, K.; Yu, H.; Liu, W.; Zhang, J.; Xing, M. Generating High-valent Iron-oxo ≡FeIV=O Complexes in Neutral Microenvironments through Peroxymonosulfate Activation by Zn−Fe Layered Double Hydroxides. *Angew. Chem., Int. Ed.* **2022**, *61* (42), e202209542.
(19) Imani, S. M.; Ladouceur, L.; Marshall, T.; Maclachlan, R.; Soleymani, L.; Didar, T. F. Antimicrobial nanomaterials and coatings: Current mechanisms and future perspectives to control the spread of viruses including SARS-CoV-2. *ACS Nano* **2020**, *14* (10), 12341−12369.
(20) Li, T.; Ge, L.; Peng, X.; Wang, W.; Zhang, W. Enhanced degradation of sulfamethoxazole by a novel Fenton-like system with significantly reduced consumption of H_2O_2 activated by g-C_3N_4/MgO composite. *Water Res.* **2021**, *190*, No. 116777.
(21) Mese, K.; Bunz, O.; Volkwein, W.; Vemulapalli, S. P. B.; Zhang, W.; Schellhorn, S.; Heenemann, K.; Rueckner, A.; Sing, A.; Vahlenkamp, T. W.; Severing, A. L.; Gao, J.; Aydin, M.; Jung, D.; Bachmann, H. S.; Zanker, K. S.; Busch, U.; Baiker, A.; Griesinger, C.; Ehrhardt, A. Enhanced antiviral function of magnesium chloride-modified heparin on a broad spectrum of viruses. *Int. J. Mol. Sci.* **2021**, *22* (18), 10075.
(22) Qin, X.; Zhang, L.; Xu, G.; Zhu, S.; Wang, Q.; Gu, M.; Zhang, X.; Sun, C.; Balbuena, P. B.; Amine, K.; Shao, M. The role of Ru in improving the activity of Pd toward hydrogen evolution and oxidation reactions in alkaline solutions. *ACS Catal.* **2019**, *9* (10), 9614−9621.
(23) Zhong, Y.; Yin, L.; He, P.; Liu, W.; Wu, Z.; Wang, H. Surface chemistry in cobalt phosphide-stabilized lithium-sulfur batteries. *J. Am. Chem. Soc.* **2018**, *140* (4), 1455−1459.
(24) Brooks, G.; Trang, S.; Witt, P.; Khan, M. N. H.; Nagle, M. The carbothermic route to magnesium. *Jom* **2006**, *58*, 51−55.
(25) Hu, F.; Pan, J.; Ma, X.; Zhang, X.; Chen, J.; Xie, W. Preparation of Mg and Ca metal by carbothermic reduction method - a thermodynamics approach. *J. Magnes. Alloy.* **2013**, *1* (3), 263−266.
(26) Fanaei, F.; Moussavi, G.; Srivastava, V.; Sillanpää, M. The enhanced catalytic potential of sulfur-doped MgO (S-MgO) nanoparticles in activation of peroxysulfates for advanced oxidation of acetaminophen. *Chem. Eng. J.* **2019**, *371*, 404−413.
(27) Yu, F.; Jia, C.; Wu, X.; Sun, L.; Shi, Z.; Teng, T.; Lin, L.; He, Z.; Gao, J.; Zhang, S.; Wang, L.; Wang, S.; Zhu, X. Rapid self-heating synthesis of Fe-based nanomaterial catalyst for advanced oxidation. *Nat. Commun.* **2023**, *14* (1), 4975.
(28) Jiang, Y.; Chen, H.; Mu, X.; He, Z. Thermal decomposition of magnesium acetate in nitrogen. *J. Phys. Conf. Ser.* **1653**, *2020*, No. 012057.
(29) Yao, Y.; Huang, Z.; Li, T.; Wang, H.; Liu, Y.; Stein, H. S.; Mao, Y.; Gao, J.; Jiao, M.; Dong, Q.; Dai, J.; Xie, P.; Xie, H.; Lacey, S. D.; Takeuchi, I.; Gregoire, J. M.; Jiang, R.; Wang, C.; Taylor, A. D.; Shahbazian-Yassar, R.; Hu, L. High-throughput, combinatorial synthesis of multimetallic nanoclusters. *Proc. Nat. Acad. Sci.* **2020**, *117* (12), 6316−6322.
(30) Li, T.; Yao, Y.; Ko, B. H.; Huang, Z.; Dong, Q.; Gao, J.; Chen, W.; Li, J.; Li, S.; Wang, X.; Shahbazian-Yassar, R.; Jiao, F.; Hu, L. Carbon-supported high-entropy oxide nanoparticles as stable electrocatalysts for oxygen reduction reactions. *Adv. Funct. Mater.* **2021**, *31* (21), 2010561.
(31) Jiang, F.; Yao, Y.; Natarajan, B.; Yang, C.; Gao, T.; Xie, H.; Wang, Y.; Xu, L.; Chen, Y.; Gilman, J.; Cui, L.; Hu, L. Ultrahigh-temperature conversion of biomass to highly conductive graphitic carbon. *Carbon* **2019**, *144*, 241−248.
(32) Sadowski, L. A.; Upadhyay, R.; Greeley, Z. W.; Margulies, B. J. Current drugs to treat infections with herpes simplex viruses-1 and −2. *Viruses* **2021**, *13* (7), 1228.
(33) Ghauch, A.; Ayoub, G.; Naim, S. Degradation of sulfamethoxazole by persulfate assisted micrometric Fe^0 in aqueous solution. *Chem. Eng. J.* **2013**, *228*, 1168−1181.
(34) Yao, Y.; Huang, Z.; Xie, P.; Lacey, S. D.; Jacob, R. J.; Xie, H.; Chen, F.; Nie, A.; Pu, T.; Rehwoldt, M.; Yu, D.; Zachariah, M. R.; Wang, C.; Shahbazian-Yassar, R.; Li, J.; Hu, L. Carbothermal shock synthesis of high-entropy-alloy nanoparticles. *Science* **2018**, *359* (6383), 1489−1494.
(35) Xiao, R.; Wang, J. J.; Li, R.; Park, J.; Meng, Y.; Zhou, B.; Pensky, S.; Zhang, Z. Enhanced sorption of hexavalent chromium [Cr(VI)] from aqueous solutions by diluted sulfuric acid-assisted MgO-coated biochar composite. *Chemosphere* **2018**, *208*, 408−416.
(36) Aravind Kumar, J.; Joshua Amarnath, D.; Anuradha Jabasingh, S.; Senthil Kumar, P.; Vijai Anand, K.; Narendrakumar, G.; Karthick Raja Namasivayam, S.; Krithiga, T.; Sunny, S.; Purna Pushkala, S.; Yuvarajan, D. One pot green synthesis of nano magnesium oxide-carbon composite: Preparation, characterization and application towards anthracene adsorption. *J. Clean. Prod.* **2019**, *237*, No. 117691.
(37) Li, L.; Hu, J.; Shi, X.; Fan, M.; Luo, J.; Wei, X. Nanoscale zero-valent metals: A review of synthesis, characterization, and applications to environmental remediation. *Environ. Sci. Pollut. Res.* **2016**, *23* (18), 17880−17900.
(38) Lee, G.; Park, J.; Harvey, O. R. Reduction of chromium(VI) mediated by zero-valent magnesium under neutral pH conditions. *Water Res.* **2013**, *47* (3), 1136−1146.
(39) Zhang, W.; Wei, P.; Chen, M.; Han, L.; Zhao, Y.; Yan, J.; Qian, L.; Gu, M.; Li, J. Trichloroethylene dechlorination rates, pathways, and efficiencies of ZVMg/C in aqueous solution. *J. Hazard. Mater.* **2021**, *417*, No. 125993.
(40) Islam, A.; Mukherjee, B.; Pandey, K. K.; Keshri, A. K. Ultra-Fast, chemical-free, mass production of high quality exfoliated graphene. *ACS Nano* **2021**, *15* (1), 1775−1784.
(41) Advincula, P. A.; Luong, D. X.; Chen, W.; Raghuraman, S.; Shahsavari, R.; Tour, J. M. Flash graphene from rubber waste. *Carbon* **2021**, *178*, 649−656.
(42) Jia, C.; Pang, M.; Lu, Y.; Liu, Y.; Zhuang, M.; Liu, B.; Lu, J.; Wei, T.; Wang, L.; Bian, T.; Wang, M.; Yu, F.; Sun, L.; Lin, L.; Teng, T.; Wu, X.; He, Z.; Gao, J.; Luo, J.; Zhang, S.; Feng, L.; Yin, X.; You, F.; Li, G.; Zhang, L.; Zhu, Y.; Zhu, X.; Yang, Y. Graphene environmental footprint greatly reduced when derived from biomass waste *via* flash Joule heating. *One Earth* **2022**, *5* (12), 1394−1403.
(43) Ren, W.; Cheng, C.; Shao, P.; Luo, X.; Zhang, H.; Wang, S.; Duan, X. Origins of electron-transfer regime in persulfate-based nonradical oxidation processes. *Environ. Sci. Technol.* **2022**, *56* (1), 78−97.
(44) He, Y.; Zhang, J.; Zhou, H.; Yao, G.; Lai, B. Synergistic multiple active species for the degradation of sulfamethoxazole by peroxymonosulfate in the presence of CuO@FeO_x@Fe^0. *Chem. Eng. J.* **2020**, *380*, No. 122568.
(45) Wang, A.; Ni, J.; Wang, W.; Wang, X.; Liu, D.; Zhu, Q. MOF-derived N-doped ZnO carbon skeleton@hierarchical Bi_2MoO_6 S-scheme heterojunction for photodegradation of SMX: Mechanism, pathways and DFT calculation. *J. Hazard. Mater.* **2022**, *426*, No. 128106.
(46) Yu, X.; Jin, X.; Wang, N.; Yu, Y.; Zhu, X.; Chen, M.; Zhong, Y.; Sun, J.; Zhu, L. Transformation of sulfamethoxazole by sulfidated nanoscale zerovalent iron activated persulfate: Mechanism and risk assessment using environmental metabolomics. *J. Hazard. Mater.* **2022**, *428*, No. 128244.
(47) Xu, M.; Li, J.; Yan, Y.; Zhao, X.; Yan, J.; Zhang, Y.; Lai, B.; Chen, X.; Song, L. Catalytic degradation of sulfamethoxazole through peroxymonosulfate activated with expanded graphite loaded $CoFe_2O_4$ particles. *Chem. Eng. J.* **2019**, *369*, 403−413.
(48) Wang, Z.; Wang, J.; Xiong, B.; Bai, F.; Wang, S.; Wan, Y.; Zhang, L.; Xie, P.; Wiesner, M. R. Application of cobalt/peracetic acid to degrade sulfamethoxazole at neutral condition: Efficiency and mechanisms. *Environ. Sci. Technol.* **2020**, *54* (1), 464−475.
(49) Tian, S.; Wang, L.; Liu, Y.; Yang, T.; Huang, Z.; Wang, X.; He, H.; Jiang, J.; Ma, J. Enhanced permanganate oxidation of sulfamethoxazole and removal of dissolved organics with biochar: Formation of highly oxidative manganese intermediate species and in situ activation of biochar. *Environ. Sci. Technol.* **2019**, *53* (9), 5282−5291.

https://doi.org/10.1021/acsestengg.3c00614
ACS EST Engg. 2024, 4, 1302−1311

(50) Sheikhi, S.; Jebalbarezi, B.; Dehghanzadeh, R.; Maryamabadi, A.; Aslani, H. Sulfamethoxazole oxidation in secondary treated effluent using Fe(VI)/PMS and Fe(VI)/H_2O_2 processes: Experimental parameters, transformation products, reaction pathways and toxicity evaluation. *J. Environ. Chem. Eng.* **2022**, *10* (3), No. 107446.
(51) Li, A.; Wu, Z.; Wang, T.; Hou, S.; Huang, B.; Kong, X.; Li, X.; Guan, Y.; Qiu, R.; Fang, J. Kinetics and mechanisms of the degradation of PPCPs by zero-valent iron (Fe degrees) activated peroxydisulfate (PDS) system in groundwater. *J. Hazard. Mater.* **2018**, *357*, 207−216.
(52) He, M. F.; Li, W. Q.; Xie, Z. H.; Yang, S. R.; He, C. S.; Xiong, Z. K.; Du, Y.; Liu, Y.; Jiang, F.; Mu, Y.; Lai, B. Peracetic acid activation by mechanochemically sulfidated zero valent iron for micropollutants degradation: Enhancement mechanism and strategy for extending applicability. *Water Res.* **2022**, *222*, No. 118887.
(53) Yan, J.; Peng, J.; Lai, L.; Ji, F.; Zhang, Y.; Lai, B.; Chen, Q.; Yao, G.; Chen, X.; Song, L. Activation $CuFe_2O_4$ by hydroxylamine for oxidation of antibiotic sulfamethoxazole. *Environ. Sci. Technol.* **2018**, *52* (24), 14302−14310.
(54) Qin, H.; Zhao, Y.; Cheng, M.; Wang, Q.; Wang, Q.; Wang, J.; Jiang, Y.; An, Z.; Zhang, X. Anti-biofilm properties of magnesium metal *via* alkaline pH. *RSC Adv.* **2015**, *5* (28), 21434−21444.
(55) Minton, K. Immunodeficiency: Magnesium regulates antiviral immunity. *Nat. Rev. Immunol.* **2013**, *13* (8), 548−549.
(56) Luganini, A.; Sibille, G.; Mognetti, B.; Sainas, S.; Pippione, A. C.; Giorgis, M.; Boschi, D.; Lolli, M. L.; Gribaudo, G. Effective deploying of a novel DHODH inhibitor against herpes simplex type 1 and type 2 replication. *Antiviral Res.* **2021**, *189*, No. 105057.
(57) Li, M. K.; Liu, Y. Y.; Wei, F.; Shen, M. X.; Zhong, Y.; Li, S.; Chen, L. J.; Ma, N.; Liu, B. Y.; Mao, Y. D.; Li, N.; Hou, W.; Xiong, H. R.; Yang, Z. Q. Antiviral activity of Arbidol hydrochloride against herpes simplex virus I in vitro and in vivo. *Int. J. Antimicrob. Agents* **2018**, *51* (1), 98−106.

https://doi.org/10.1021/acsestengg.3c00614
ACS EST Engg. 2024, 4, 1302−1311